Speed Up of an Analytical Algorithm for Nonuniform Attenuation Correction by Using PC Video/Graphics Card Architecture

Junhai Wen, *Member, IEEE*, Zigang Wang, *Member, IEEE*, Bin Li, Tianfang Li, *Member, IEEE*, and Zhengrong Liang, *Member, IEEE*

***Abstract*—A major task in quantitative SPECT (single photon emission computed tomography) reconstruction is compensation for object-specific attenuation, which is usually nonuniform. Mathematically this task is expressed as the inversion of the attenuated Radon transform. Novikov had derived an explicit inversion formula for the attenuated Radon transform for parallel-beam collimation geometry. In our previous work, we extended his work to variable focusing fan-beam (VFF) collimators. A ray-driven analytical inversion formula for VFF reconstruction with nonuniform attenuation was derived. The drawback of ray-driven methods is that they are time consuming. In this work, we proposed a fast implementation method, which includes algorithm optimization and acceleration by the texture-mapping architecture of PC graphics/video card. We further investigated the noise properties and associated artifacts of the analytical inversion formula. The artifacts were remarkably reduced when more projections were sampled to mitigate the problem of wide bandwidth of the discrete Hilbert transform. The reconstruction from noisy data demonstrated the accuracy and robustness of the presented ray-driven analytical inversion formula with dramatic speed acceleration by the PC graphics/video card.**

***Index Terms*—Analytical reconstruction, nonuniform attenuation, PC video/graphics card, ray driven, speed up.**

I. Introduction

In single-photon emission computed tomography (SPECT) imaging, because of photoelectric absorption and Compton scatter, the gamma photons of the intravenously injected radiotracer are attenuated inside the body before arriving at the detector. Quantitative reconstruction of the radiotracer uptake concentration at any location inside the body requires accurate compensation for the body's object-specific attenuation, which is usually nonuniform. Mathematically, the compensation and reconstruction task can be formulated as the inversion of the attenuated Radon transform [1]. A great research interest in analytical inversion of the attenuated Radon transform for quantitative SPECT image reconstruction with nonuniform attenuation and parallel-beam geometry has been seen in the last decade. Arbuzov *et al.* [2] presented an inversion of the attenuated Radon transform, but their result was not cast in the well-established filtered backprojection (FBP) form [3], [4], which was later derived by Novikov [5]. In Novikov's work, an explicit inversion formula was derived in the FBP form for the attenuated Radon transform with parallel-beam geometry. This formula was implemented and good reconstruction results were obtained [6]. Another version of the explicit inversion formula was later reported by Natterer [7], also for parallel-beam geometry.

For many clinical applications, however, fan-beam and variable focusing fan-beam (VFF) collimation geometries are preferred. Fan-beam collimator improves count density and spatial resolution, as compared to parallel-beam collimator, for imaging small objects such as animals and human head and breasts. An analytical inversion of the attenuated Radon transform for fan-beam geometry was recently reported, with some assumptions and approximations [8]. For cardiac studies, however, the fan-beam geometry encounters the truncation problem due to its limited acceptance angle across the field-of-view (FOV), which can cause artifacts in the reconstructed SPECT images. Variable focusing fan-beam collimator overcomes this truncation problem, while preserving the improved count density and spatial resolution [9]–[11].

In our previous work, we derived an approximate inversion formula for the attenuated Radon transform for both fan-beam and VFF collimator geometries and obtained very good reconstruction results [12], [13]. An exact ray-driven analytical formula for fan-beam reconstruction with nonuniform attenuation was obtained in [14] and for VFF reconstruction with nonuniform attenuation in [15]. But the drawback of ray-driven methods is that they are time consuming. In this work, we propose a fast implementation method, which includes algorithm optimization and acceleration by the texture-mapping architecture of PC graphics/video card. We further investigated the noise properties and associated artifacts of the analytical inversion formula.

II. The Ray-Driven Method for Inversion of the Nonuniformly Attenuated Radon Transform With VFF Collimators

In SPECT imaging, the measured projection data at angle ϕ can be expressed as

$$g_\phi(x_r) = \int_{-\infty}^{\infty} \exp[-(D_\phi a_\phi)(x_r, y_r)] f_\phi(x_r, y_r) dy_r \qquad (1)$$

Manuscript received November 12, 2003; revised April 7, 2004. This work was supported in part by the NIH National Heart, Lung, and Blood Institute under Grant HL54166.

J. Wen, Z. Wang, and B. Li are with the Department of Radiology, State University of New York, Stony Brook, NY 11794 USA (e-mail: wenjh@mil.sunysb.edu).

T. Li is with the Department of Physics and Astronomy, State University of New York, Stony Brook, NY 11794 USA.

Z. Liang is with the Departments of Radiology and Computer Science, State University of New York, Stony Brook, NY 11794 USA.

Digital Object Identifier 10.1109/TNS.2004.829788

where $f(x,y)$ denotes the activity source distribution to be reconstructed and $a(x,y)$ is the nonuniform attenuation coefficient map across the body. $f_\phi(x,y)$ and $a_\phi(x,y)$ are the rotated activity distribution and the rotated attenuation map with rotation angle ϕ. Note that $g_\phi(x_r)$ is the projection datum at position x_r with projection angle ϕ. The relation between the stationary coordinates (x,y) and the rotated coordinates (x_r,y_r) is

$$\begin{aligned} x_r &= x\cos\phi + y\sin\phi \\ y_r &= -x\sin\phi + y\cos\phi. \end{aligned} \tag{2}$$

The divergent beam transform is

$$\begin{aligned} (D_\phi a_\phi)(x_r,y_r) &= D_\phi\{a_\phi(x_r,y_r)\} \\ &= \int_{y_r}^{\text{det ector}} a_\phi(x_r,y_r')\,dy_r'. \end{aligned} \tag{3}$$

In SPECT, the gamma photons are attenuated before arriving at the detector, so $\exp[-(D_\phi a_\phi)(x_r,y_r)]$ reflects the attenuation of gamma photons emitted from point (x_r,y_r) before arriving at the detector with angle ϕ.

Based on Novikov's parallel-beam reconstruction formula, we obtained the ray-driven reconstruction formulas for parallel-beam geometry with nonuniform attenuation [15]

$$f(x,y) = \frac{1}{4\pi}\left(\frac{\partial}{\partial x}B_C(x,y) + \frac{\partial}{\partial y}B_S(x,y)\right) \tag{4}$$

and

$$\begin{aligned} B_C(x,y) &= \int_0^{2\pi}\int_{-\infty}^{\infty}\left[e^{(D_\phi a_\phi)(x_r,y_r)} g a_{(\phi,x_r'')}(x_r)\right] \\ &\quad\times\cos\phi\, dx_r''\, d\phi \\ B_S(x,y) &= \int_0^{2\pi}\int_{-\infty}^{\infty}\left[e^{(D_\phi a_\phi)(x_r,y_r)} g a_{(\phi,x_r'')}(x_r)\right] \\ &\quad\times\sin\phi\, dx_r''\, d\phi \end{aligned} \tag{5}$$

where

$$\begin{aligned} &g a_{(\phi,x_r'')}(x_r) \\ &\quad= e^{-A_\phi(x_r)}\Big[\cos(E_\phi(x_r)) \\ &\qquad\times H\left\{\cos(E_\phi(x_r''))e^{A_\phi(x_r'')} g_\phi(x_r'')\delta(x_r - x_r'')\right\} \\ &\qquad+\sin(E_\phi(x_r)) \\ &\qquad\times H\left\{\sin(E_\phi(x_r''))e^{A_\phi(x_r'')} g_\phi(x_r'')\delta(x_r - x_r'')\right\}\Big] \\ &E_\phi(u) = H\{A_\phi(u)\}, \quad \text{and} \quad A_\phi(u) = \frac{1}{2}R_\phi\{a_\phi(u,v)\} \end{aligned} \tag{6}$$

and $g a_{(\phi,x_r'')}(x_r)$ can be seen as the reconstruction contribution of ray (ϕ,x_r'') at projection position x_r. R represents the Radon transform and H denotes the Hilbert transform.

Note that any ray (p,β) in the VFF geometry can be seen as a ray (x_r,ϕ) in the parallel-beam geometry (see Fig. 1 below). Let $D(p)$ be the variable focal length. The relation between the parallel-beam and VFF-beam geometries is

$$\begin{aligned} \phi &= \beta + \gamma = \beta + \arctan\frac{p}{D(p)} \\ x_r &= p\cos\gamma = \frac{pD(p)}{\sqrt{D(p)^2+p^2}}. \end{aligned} \tag{7}$$

For each ray (p,β), we can build a local coordinate system (u,v). The relation between this local coordinate system and the original coordinate system is

$$\begin{aligned} u &= x\cos\phi + y\sin\phi \\ v &= -x\sin\phi + y\cos\phi. \end{aligned} \tag{8}$$

In this local coordinate system, ray (p,β) can be seen as a parallel-beam ray. So we can use our parallel-beam ray-driven reconstruction formula to calculate the reconstruction contribution of this ray for every reconstruction point in the image domain. For any point (x,y), its position in this local coordinate system is (u,v).

In summary, our ray-driven analytical VFF reconstruction formula can be expressed as

$$f(x,y) = \frac{1}{4\pi}\left(\frac{\partial}{\partial x}B_C(x,y) + \frac{\partial}{\partial y}B_S(x,y)\right) \tag{9}$$

$$\begin{aligned} B_C(x,y) &= \int_0^{2\pi}\int_{-\infty}^{\infty}\left[e^{(D_\phi a_\phi)(u,v)} g a_{(\beta,p)}(u)\right]\cos\phi|J|\, dp\, d\beta \\ B_S(x,y) &= \int_0^{2\pi}\int_{-\infty}^{\infty}\left[e^{(D_\phi a_\phi)(u,v)} g a_{(\beta,p)}(u)\right]\sin\phi|J|\, dp\, d\beta \end{aligned} \tag{10}$$

where the Jacobian $|J|$ is given by

$$|J| = \begin{vmatrix} \partial x_r/\partial p & \partial x_r/\partial\beta \\ \partial\phi/\partial p & \partial\phi/\partial\beta \end{vmatrix} = \frac{D^3(p)+p^3D'(p)}{\sqrt{(D^2(p)+p^2)^3}}$$

and

$$\begin{aligned} &g a_{(\beta,p)}(u) \\ &\quad= e^{-A_\phi(u)}\Big[\cos(E_\phi(u)) \\ &\qquad\times H\left\{\cos(E_\phi(x_r))e^{A_\phi(x_r)} g(p,\beta)\delta(u-x_r)\right\} \\ &\qquad+\sin(E_\phi(u)) \\ &\qquad\times H\left\{\sin(E_\phi(x_r))e^{A_\phi(x_r)} g(p,\beta)\delta(u-x_r)\right\}\Big] \\ &E_\phi(u) = H\{A_\phi(u)\}, \quad \text{and} \quad A_\phi(u) = \frac{1}{2}R_\phi\{a_\phi(u,v)\} \end{aligned} \tag{11}$$

where $g(p,\beta)$ is VFF projection datum at position p with projection angle β. The relation between (x,y) and (u,v) is shown by (8). The relation between (p,β) and (x_r,ϕ) is shown by (7). Therefore, (u,v) can be determined by (x,y), and (x_r,ϕ) can be obtained from (p,β).

Each ray in the local coordinate system can be seen as a parallel-beam ray, with position (x_r,ϕ). Using (10) and (11), the reconstruction contributions of this ray to every reconstruction point across the FOV is calculated and then backprojected to

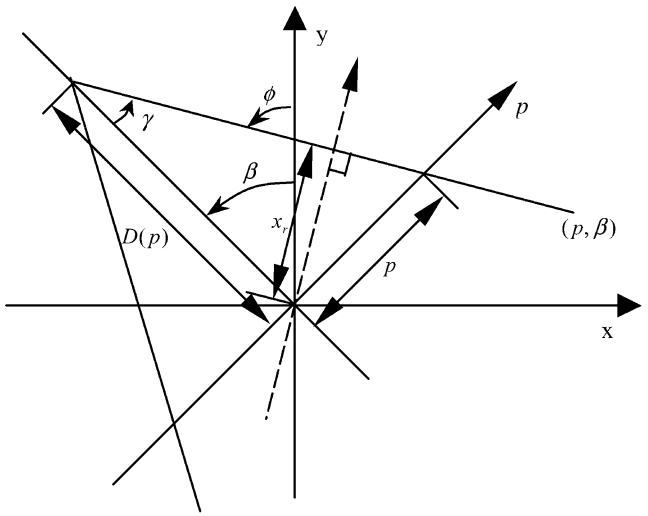

Fig. 1. The relation between parallel-beam and VFF geometries.

these reconstruction points with different weights according to the equations. After all VFF rays are calculated in a ray-by-ray manner, two images $B_c(x,y)$ and $B_s(x,y)$ are obtained, i.e., $(B_c(x,y), B_s(x,y))$ is a vector image. By using (9), the final image is then reconstructed.

III. Fast Implementation Method for the Ray-Driven Reconstruction With Nonuniform Attenuation

Our reconstruction algorithm is based on a ray-driven strategy. The drawback of ray-driven methods is that they are time consuming. Therefore, a fast implementation method is proposed to mitigate the computing burden. If the attenuation map is fixed for a reconstruction, we may calculate the reconstruction contributions of every ray for every reconstruction point in advance (see Fig. 2), and save them into a database or disk space for reuse. If the size of the reconstructed image is $K \times K$, the number of projections is M and the number of bins of each projection is N, we need $M \times N$ contribution images to be saved in the database. When performing the reconstruction, we only need to load the database and multiply it by the corresponding rays, and then add the contribution images of all rays together, with different weights of $\cos\phi$ or $\sin\phi$. The results are $B_C(x,y)$ and $B_S(x,y)$. If the attenuation map is different for different reconstructions, it is not necessary to save the contribution images. We just need to multiply them by weights $(\cos\phi, \sin\phi)$ and sum the results into $B_C(x,y)$ and $B_S(x,y)$ (see Fig. 3). The final image is reconstructed by the use of (9).

For ray (p,β), its reconstruction contribution image is

$$C_{(\beta,p)}(x,y) = \left[e^{(D_\phi a_\phi)(u,v)} g a_{(\beta,p)}(u)\right] |J| \qquad (12)$$

where

$$\begin{aligned} & g a_{(\beta,p)}(u) \\ &= e^{-A_\phi(u)} \left[\cos(E_\phi(u)) H\left\{\cos(E_\phi(x_r)) e^{A_\phi(x_r)} \delta(u-x_r)\right\}\right. \\ &\quad \left. + \sin(E_\phi(u)) H\left\{\sin(E_\phi(x_r)) e^{A_\phi(x_r)} \delta(u-x_r)\right\}\right] \\ & E_\phi(u) = H\{A_\phi(u)\}, \quad \text{and} \quad A_\phi(u) = \frac{1}{2} R_\phi\{a_\phi(u,v)\}. \end{aligned} \qquad (13)$$

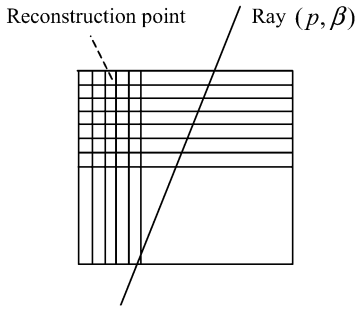

Fig. 2. Reconstruction point and ray.

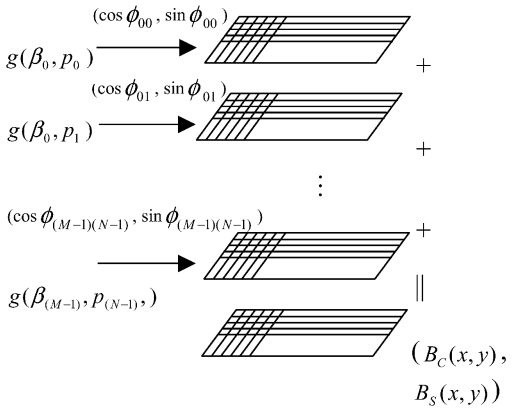

Fig. 3. Fast reconstruction of ray-driven algorithm.

If the number of projections is M and the number of bins of each projection is N, we have $M \times N$ contribution images

$$C_{(\beta_i,p_j)}(x,y), i = 0,1,\ldots,M-1; j = 0,1,\ldots,N-1. \qquad (14)$$

When performing the reconstruction, we only need to load these contribution images. The reconstruction is given by

$$f(x,y) = \frac{1}{4\pi}\left(\frac{\partial}{\partial x} B_C(x,y) + \frac{\partial}{\partial y} B_S(x,y)\right) \qquad (15)$$

$$B_C(x,y) = \sum_{i=0}^{M-1}\sum_{j=0}^{N-1} g(\beta_i,p_j) C_{(\beta_i,p_j)}(x,y)\cos\phi_{i,j}\Delta p\Delta\beta$$

$$B_S(x,y) = \sum_{i=0}^{M-1}\sum_{j=0}^{N-1} g(\beta_i,p_j) C_{(\beta_i,p_j)}(x,y)\sin\phi_{i,j}\Delta p\Delta\beta \qquad (16)$$

where

$$\phi_{i,j} = \beta_i + \arctan\frac{p_j}{D(p_j)} \qquad (17)$$

and $g(\beta_i,p_j)$ represents the projection data.

IV. Accelerating Image Reconstruction by Hardware Technologies

Due to the large number of rotation and interpolation operations in the above presented ray-driven reconstruction algorithm, the computation is time intensive for currently available PC CPU and RAM capacities. The computational burden could be reduced by more powerful computers available in the future. In this paper, we explored an alternative means.

Due to drive force of the game marketing and 3-D image rendering, the PC graphics/video card has been developed to handle a large dataset in a real-time manner, in a similar way as that used in a supercomputer graphics engine. The 2-D/3-D texture mapping architecture is readily available to speed up the operations. We implemented the presented reconstruction algorithm on a Windows 2000 operating system, on a PC platform of a Pentium 4 with a CPU speed of 1.7 GHz and memory of 1.0 GB RAM, and an Nvidia@ Geforce3 graphics board of 64 MB RAM (current cost of less than $200).

Texture mapping was a well-developed tool in the computer graphics field in the 1980s [16]. Now 2-D texture mapping has already become a standard technique that can be implemented by standard graphics card on PC. With the development of the GPU (graphics processor utility) and video memory, current graphics cards can implement 3-D texture mapping and multiple texture mapping. Furthermore, current graphics cards support the 2-D/3-D texture with 32 bit precision. This means that more and more information can be stored in the texture. With powerful GPU and advanced texture mapping techniques, modern graphics cards can take over many image processing jobs, which usually could only be performed by the CPU. Due to the specific design of the GPU, it can now perform many image processing operations, such as rotation and convolution, at a speed much faster than the CPU.

The core idea of the texture mapping is to paste 2-D/3-D images on a polygon in 3-D space. When the polygon is rotated, the corresponding images will be rotated as well. Using the projection matrix, each voxel on the polygon will be projected onto a 2-D plane. The texture mapping technique was adapted to perform the rotation and interpolation operations in the above presented ray-driven reconstruction algorithm. The proposed algorithm was written using the OpenGL graphical program language. At first, we defined the attenuation map as a 2-D texture using the function glTexImage2-D(). Thus, the whole attenuation map was loaded into the texture unit of the graphic card. Using the function glTexCoord(), we pasted the attenuation map onto a 2-D square. For each ray, we used the function glRotated() to rotate the square in order to make this ray to be a parallel-beam ray. Correspondingly, the attenuation map image that was pasted on this square would be rotated at the same time. Using a projection matrix, a new map image, representing the rotated attenuation map, could be obtained using the function glReadPixels(). All the interpolation and the re-sampling of the voxel values are done by the GPU in parallel. It usually takes only several milliseconds to finish this procedure, which may take several seconds in the CPU.

Multiple texture mapping technique is a new technique that was developed in 1990s. This technique allows the user to paste several texture images on a given polygon at the same time. Modern graphics cards support up to 16 textures on a polygon at one time. For each point in the polygon, the modern graphics card can provide some programmable operations such as addition, multiplication, and etc. This technique was utilized in this work to accelerate the back-projection for each ray. First, we mapped two images—the local attenuation coefficient map and the weight map—on one polygon. Then two textures were rotated to their original angles and multiplied together. Since all these rotation and multiple operations are implemented by the GPU, it only takes several milliseconds to perform all the operations for the whole images. This improves the reconstruction speed dramatically.

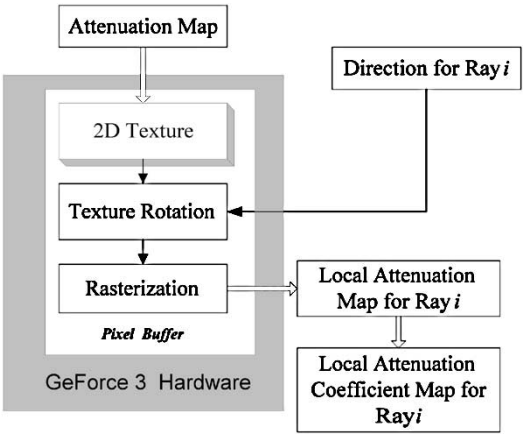

Fig. 4. The flowchart of hardware acceleration on the rotation and re-sampling of the attenuation map.

The implementation of the above image reconstruction operations is similar to that of accelerated rendering of 3-D image datasets. A modern graphics card provides a flexible and programmable hardware means to implement the 3-D transverse and texture processing for image rendering. For example, the Nvidia@ Geforce3 graphics card supports multitexture and "texture shader" technologies for programmable texture processing. Using these technologies, our reconstruction algorithm was accelerated in two stages below.

A. Rotation of the Attenuation Map

In our ray-driven reconstruction algorithm, the attenuation map needs to be rotated and re-sampled for each ray. These two operations are time consuming. At this first stage, the rotation and re-sampling of the attenuation map were implemented by a traditional graphics pipeline with hardware acceleration (see Fig. 4). Because of the precision limitation of our Geforce3 graphics card, after obtaining the local attenuation map $a_\phi(x_r, y_y)$, we calculated the local attenuation coefficient maps $(D_\phi a_\phi)(x_r, y_r)$ and $\exp\{(D_\phi a_\phi)(x_r, y_r)\}$ in the CPU, not in the graphics card. With a new, more costly graphics card, we can calculate these two parts in the graphics card, which would further improve the reconstruction speed.

B. Back-Projection Operation

For each ray, the local attenuation coefficient map generated by the first stage above and the corresponding weighted map needed to be rotated to its original angle for implementation of (12). The multitexture operations, such as addition and multiplication, were used for this task (see Fig. 5). Because there are several exponential operations in (12), which are not supported by the Geforce3 GPU, we employed the CPU to perform these exponential operations while other operations were executed on the graphics card.

By using the PC video-card hardware acceleration, the whole reconstruction time was reduced from the original 30 min to less

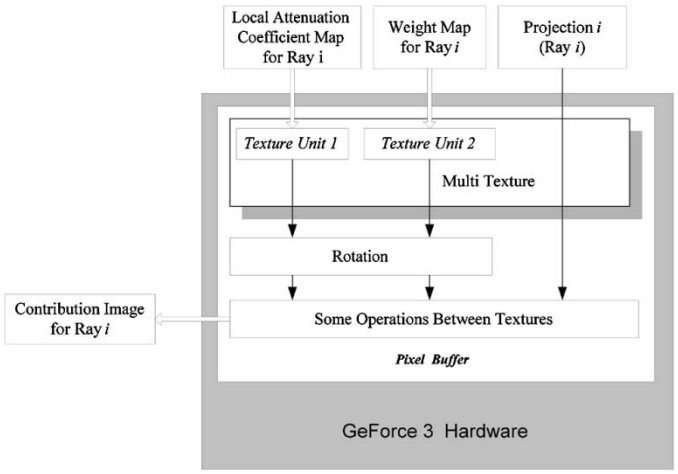

Fig. 5. The flowchart of hardware acceleration on the backprojection.

than 3 min, which includes the time for calculating the contribution images of all rays and for performing the final image reconstruction. A more than tenfold reduction of computing time was achieved.

V. The Artifact Properties in the Ray-Driven Reconstruction With Non-Uniform Attenuation

In the ray-driven image reconstruction for nonuniform attenuation, the projection along each ray is a point. This requires that the involved discrete Hilbert transform have a wide bandwidth. But this wide bandwidth requirement usually does not provide a smooth property in the spatial domain, and then causes some artifacts in the reconstructed images [6], [12]–[15]. In this work, we investigated the property of these artifacts, and found that if more projections were acquired or a higher angular sampling rate was applied, artifacts in the reconstructed images could be remarkably reduced (see Fig. 6). In Fig. 6, picture (a) is the activity phantom. Picture (b) is the attenuation map. Pictures (c) and (d) are the reconstructed images from VFF projections of 128 views, each with 128 bins, and of 256 views, each with 128 bins, respectively. The focal length function has a form of $\mathrm{D(p)} = 300 + 30|p|$ in pixel units. It is observed that when a higher angular sampling rate was applied, a reconstruction with fewer artifacts was generated. Pictures (e) and (f) are the reconstructed images from fan-beam projections of 128 views, each with 128 bins, and of 256 views, each with 128 bins, respectively. The focal length is $\mathrm{D} = 300$ in pixel units. The same trend of generating the artifacts was seen in both fan-bean and VFF reconstruction results. This observation concurs with that in the parallel-beam image reconstruction results [5]–[7], indicating that the discrete Hilbert transform needs special attention in implementation.

VI. The Noise Properties in the Ray-Driven Reconstruction With Nonuniform Attenuation

In addition to the noise-free simulation study above, noisy cases were studied to investigate the noise properties in the ray-driven reconstruction with nonuniform attenuation, in which Poisson noise with two count-density levels was added to the noise-free VFF projection data of 256 views, each with 128 bins. Fig. 7 shows the reconstruction results and the corresponding profiles along the central horizontal line. These results demonstrated the accuracy and robustness of the presented ray-driven analytical image reconstruction for nonuniform attenuating media.

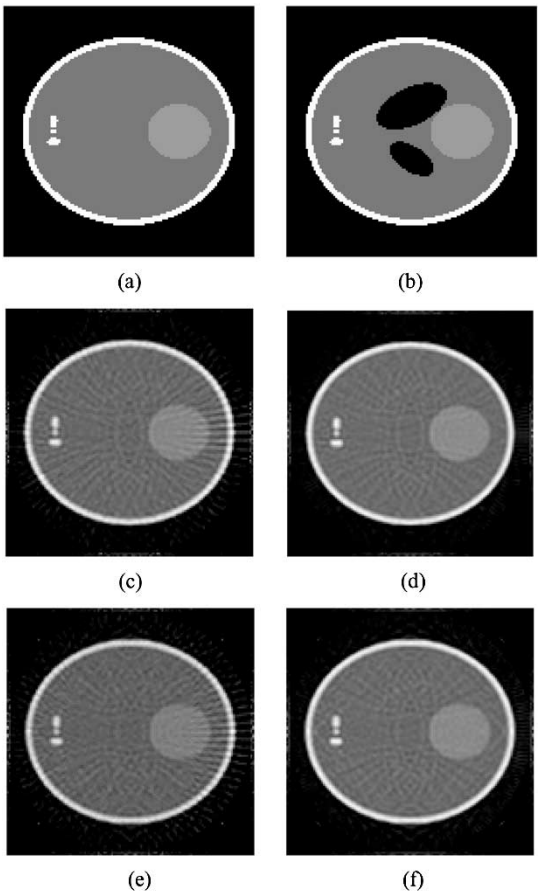

Fig. 6. Reconstruction results with different angular sampling rates. (a) The activity phantom. (b) The attenuation map. (c) The reconstructed image from VFF projections of 128 views each with 128 bins. (d) The reconstructed image from VFF projections of 256 views each with 128 bins. The focal length is $\mathrm{D(p)} = 300 + 30|\mathrm{p}|$, in pixel units. (e) The reconstructed image from fan-beam projections of 128 views each with 128 bins. (f) The reconstructed image from fan-beam projections of 256 views, each with 128 bins. The focal length is $\mathrm{D} = 300$ in pixel units.

VII. Conclusion

In this work, we proposed a fast implementation method for a ray-driven image reconstruction algorithm on the inversion of the attenuated Radon transform. If the attenuation map is fixed for a group of studies, we may calculate the reconstruction contributions of each ray for all associated reconstruction points across the FOV in advance and save them into a database or disk space for reuse. When performing the image reconstruction, we load the database, multiply it by the corresponding rays, and add the contributions of all rays together. If the attenuation map is different for different reconstructions, it is not necessary to save the contribution images. In this case, we just need to multiply them with their associated weights and sum them together. The final image is then computed efficiently by a

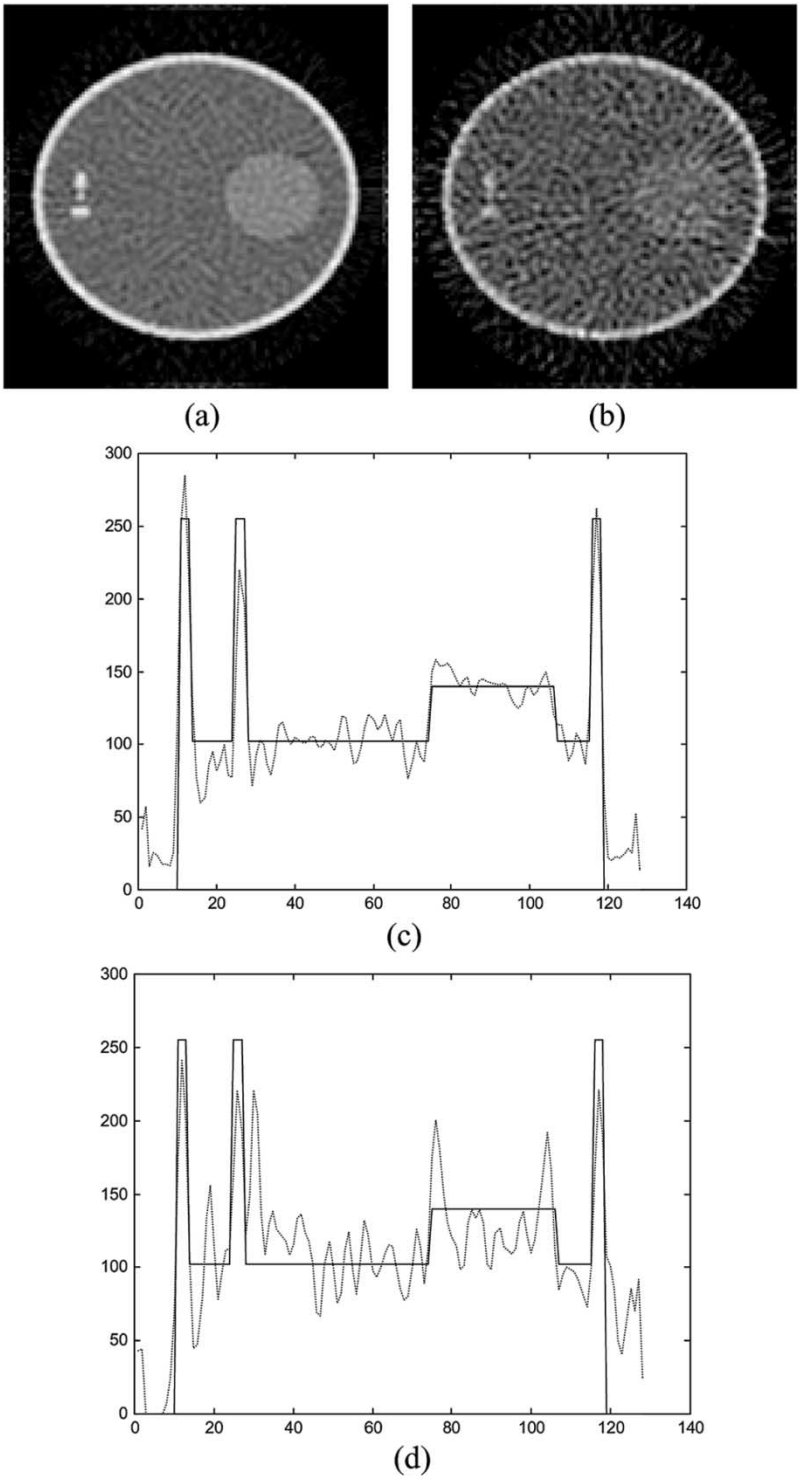

Fig. 7. Reconstruction from noisy projection data. (a) VFF $D(p) = 300 + 30|p|$ (total counts per view is 100 k). (b) VFF $D(p) = 300 + 30|p|$ (total counts per view is 10 k). (c) Profile of image (a) along the horizontal central line (where solid line is from the phantom). (d) Profile of image (b) along the horizontal central line.

divergence equation from these contributions. In addition to the above algorithm optimization on fast CPU and memory, we explored the capability of PC graphics/video card to accelerate the reconstruction speed. A more than tenfold reduction of computing time was observed with the use of the hardware, which is a necessary part of any PC platform and cost currently less than $200.

We also investigated the noise properties and the associated artifacts in the reconstruction. The artifacts were remarkably reduced when a higher angular sampling rate was used to mitigate the problem of wide bandwidth of the discrete Hilbert transform. The reconstruction results from noisy projections at two different count levels demonstrated the accuracy and robustness of the presented ray-driven analytical image reconstruction for

nonuniform attenuating media. Further investigations on artifact properties and noise propagation are currently under progress [17].

REFERENCES

[1] G. T. Gullberg, "The Attenuated Radon Transform: Theory and Application in Medicine and Biology," Ph.D. dissertation, Univ. California, Berkeley, CA, 1979.

[2] E. V. Arbuzov, A. L. Bukhgeim, and S. G. Kazantsev, "Two-dimensional tomography problems and the theory of A-analytic functions," *Siberian Adv. Math.*, vol. 8, no. 4, pp. 1–20, 1998.

[3] L. Shepp and B. Logan, "The Fourier reconstruction of a head section," *IEEE Trans. Nucl. Sci.*, vol. NS-21, pp. 21–43, 1974.

[4] G. Herman, *Image Reconstruction from Projections*. New York: Academic, 1980.

[5] R. Novikov, "An inversion formula for the attenuated X-ray transformation," *Ark. Math.*, vol. 40, pp. 145–167, 2002.

[6] L. Kunyansky, "A new SPECT reconstruction algorithm based on the Novikov's explicit inversion formula," *Inverse Problems*, vol. 17, pp. 293–306, 2001.

[7] F. Natterer, "Inversion of the attenuated Radon transform," *Inverse Problems*, vol. 17, pp. 113–119, 2001.

[8] A. A. Bukhgeim and S. G. Kazantsev, "Inversion formula for the fan-beam attenuated radon transform in a unit disk," in *Novosibirsk*, 2002. Preprint.

[9] P. C. Hawman, J. Hsieh, and B. E. Hasselquist, "The cardiofocal collimator: A novel focusing collimator for cardiac SPECT" (in abstract), *J. Nucl. Med.*, vol. 33, p. 852, 1992.

[10] G. L. Zeng, G. T. Gullberg, R. J. Jaszczak, and J. Li, "Fan-beam reconstruction algorithm for a spatially varying focal length collimator," *IEEE Trans. Med. Imaging*, vol. 12, pp. 575–582, 1993.

[11] G. L. Zeng and G. T. Gullberg, "A backprojection filtering algorithm for a spatially varying focal length collimator," *IEEE Trans. Med. Imaging*, vol. 13, pp. 549–556, 1994.

[12] J. Wen, T. Li, X. Li, and Z. Liang, "Fan-beam and variable-focal-length fan-beam SPECT reconstruction with nonuniform attenuation" (in abstract), *J. Nucl. Med. Technol.*, vol. 30, p. 97P, 2002.

[13] J. Wen, H. Lu, T. Li, and Z. Liang, "Analytical solution to 3D SPECT reconstruction with nonuniform attenuation and distance-dependent resolution variation for variable focal-length fan-beam collimators," *SPIE Med. Imaging*, vol. 5032, pp. 1858–1867, 2003.

[14] J. Wen, T. Li, and Z. Liang, "Ray-driven analytical fan-beam SPECT reconstruction with nonuniform attenuation," in *Proc. IEEE Int. Symp. Biomedical Imaging*, Washington, 2002, pp. 629–632.

[15] ——, "An analytical inversion of nonuniformly attenuated Radon transform with variable focal-length fan-beam collimators," *IEEE Trans. Nucl. Sci.*, vol. 50, pp. 1541–1549, Oct. 2003.

[16] A. Watt, "Mapping techniques," in *3D Computer Graphics*, 3rd ed. Reading, MA: Addison-Wesley, 2000, ch. 8.

[17] J. Wen, T. Li, and Z. Liang, "An analytical SPECT reconstruction strategy for extending parallel to nonparallel geometries using ray-driven technique," *J. Nucl. Med.*, vol. 44, pp. 272–273, 2003.